Atomic Layer Deposition of Bismuth Vanadates for Solar Energy Materials

Morgan Stefik*[a]

The fabrication of porous nanocomposites is key to the advancement of energy conversion and storage devices that interface with electrolytes. Bismuth vanadate, $BiVO_4$, is a promising oxide for solar water splitting where the controlled fabrication of $BiVO_4$ layers within porous, conducting scaffolds has remained a challenge. Here, the atomic layer deposition of bismuth vanadates is reported from $BiPh_3$, vanadium(V) oxytriisopropoxide, and water. The resulting films have tunable stoichiometry and may be crystallized to form the photoactive scheelite structure of $BiVO_4$. A selective etching process was used with vanadium-rich depositions to enable the synthesis of phase-pure $BiVO_4$ after spinodal decomposition. $BiVO_4$ thin films were measured for photoelectrochemical performance under AM 1.5 illumination. The average photocurrents were 1.17 $mA\,cm^{-2}$ at 1.23 V versus the reversible hydrogen electrode using a hole-scavenging sulfite electrolyte. The capability to deposit conformal bismuth vanadates will enable a new generation of nanocomposite architectures for solar water splitting.

Introduction

Atomic layer deposition (ALD) has rapidly accelerated nanomaterial development for advanced photoelectrochemical devices owing to its capability to grow ultrathin, conformal, and uniform films on flat and high-aspect-ratio structures.[1–6] ALD is based upon the sequential exposure of a substrate to pulses of gas phase precursors that each react with the substrate surface in a self-limiting manner. Typically, two reactants are used to deposit binary compounds such as M_xO_y where, for example, [M–O] cycles of metal and oxidant pulses are repeated to deposit conformal nanoscale layers. These capabilities have enabled significant progress for Fe_2O_3,[7–26] Cu_2O,[27–30] and other photoelectrodes.[6,31,32] There is a significant design advantage to using composite host–guest nanostructures for light-harvesting materials with low carrier mobilities. In this design, a "host" scaffold transports majority carriers to the substrate and the "guest" absorber transports minority carriers to the water/catalyst interface.[8,22,33–40] Noticeably absent from the literature is the ALD growth of bismuth vanadates, a class of compounds with various Bi:V ratios[41] with broad applications as pyroelectrics,[42] ferroelectrics,[43,44] and high-performance photoanodes for solar water splitting with considerable recent advancements.[45–49] Monoclinic scheelite $BiVO_4$ was first demonstrated for photoelectrochemical (PEC) water oxidation in 1998.[50] $BiVO_4$ has a moderate band gap of roughly 2.4 eV,[51] a conduction band edge of about 0 V versus reversible hydrogen electrode (RHE)[52] positioned near the H_2 evolution potential, and an appropriate valence band position for O_2 evolution. These band positions enable efficient photoassisted electrochemical water oxidation (O_2 evolution) with a low onset potential of approximately 0.25 V versus RHE.

The ALD of bismuth vanadates is a key step towards its development into host–guest composite nanostructures. Host–guest architectures have been attempted with $BiVO_4$; however, all reports suffered from either non-uniform depositions[38–40,48] or used cathodic deposition[49] that limited the use of hole-blocking layers at the interface of the host and the guest.[21,53] Here, ALD brings a significant advantage in that controlled films may be grown on arbitrary 3D porous scaffolds.

Ternary oxides have been broadly synthesized by mixing ALD recipes for the two corresponding binary oxides. Numerous bismuth precursors have been examined for ALD with limited demonstrations of the binary oxide Bi_2O_3.[54,55] Although a triphenylbismuth ($BiPh_3$) and water (W) cycle [$BiPh_3$–W] have not enabled the ALD of Bi_2O_3, the addition of a titanium(IV) isopropoxide (TTIP) and water with a [$BiPh_3$–W–TTIP–W] cycle was previously shown to enable the synthesis of mixed bismuth titanates of variable composition.[56] This behavior was attributed to a catalytic effect of the preceding pulses on the $BiPh_3$ deposition. Here, a catalytic effect of vanadium(V) oxytriisopropoxide (VTIP) on the subsequent deposition from $BiPh_3$ enables the first ALD of bismuth vanadates. Post processing of these films led to phase-pure and photoactive $BiVO_4$ with the scheelite crystal structure.

Results and Discussion

The ALD of Bi_2O_3 and V_2O_5 binary oxides were examined before developing more complex ternary procedures. As previously noted,[56] it was confirmed that $BiPh_3$ and water alone did

[a] *Prof. M. Stefik*
Department of Chemistry and Biochemistry
University of South Carolina
Columbia, SC 29208 (USA)
E-mail: morgan@stefikgroup.com

Supporting Information for this article can be found under http://dx.doi.org/10.1002/cssc.201600457.

© 2016 Wiley-VCH Verlag GmbH & Co. KGaA, Weinheim

not result in film growth over a range of deposition parameters in the ALD reactor. Also, consistent with prior reports,[57] it was established that VTIP and water were found to yield self-limiting ALD growth at a rate of 0.22 Å per cycle at a reactor temperature of 130 °C (Figure 1). A quartz crystal microbalance array was used to monitor depositions in situ to efficiently explore the extensive parameter space. The VTIP pulse length was optimized for the large ALD reactor where a 2 s pulse of VTIP was required to saturate the growth rate per cycle with the expected ~0.2 Å per cycle rate (Figure 2 a).[58] Also similar to prior V_2O_5 ALD work, an extended exposure to water vapor was used to encourage hydrolysis of isopropoxy ligands. Here, an extended 1 s exposure was used with the reactor isolated from the vacuum pump before purging (see the Experimental Section) rather than a continuous pulse of oxidant. Indeed, pulses longer than 25 ms required extensive purging for 30–60 s to avoid uncontrolled chemical vapor deposition (CVD). A ~25 ms water pulse resulted in a saturated growth rate within the error of the measurement (Figure 2 b). The slow growth rate of V_2O_5 motivates the use of time-efficient protocols. The effect of purging conditions was extensively explored where high purge flow rates had a more significant effect than total purge time (data not shown). Using a maximum 200 sccm nitrogen flow rate of the reaction the purge time

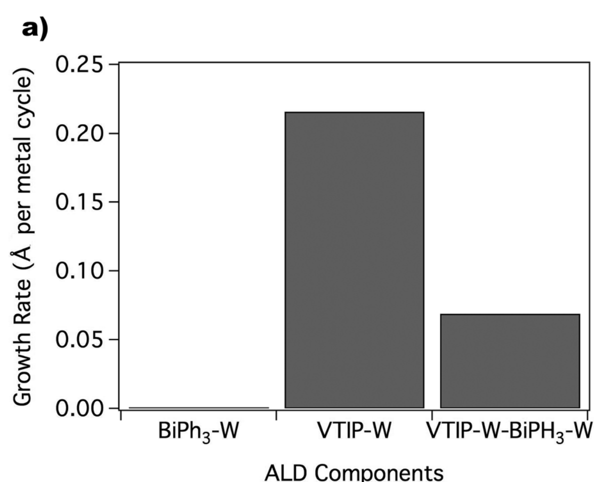

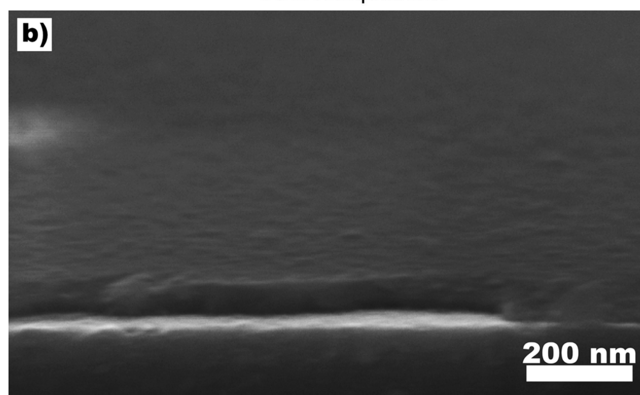

Figure 1. a) Growth rates for binary oxides of Bi_2O_3 from [$BiPh_3$–W], and V_2O_5 from [VTIP–W] as well as the associated bismuth vanadate ternary from [VTIP–W-$BiPh_3$–W]. b) SEM cross-section of [VTIP–W–$BiPh_3$–W]$_{4000}$ deposited on a Si wafer.

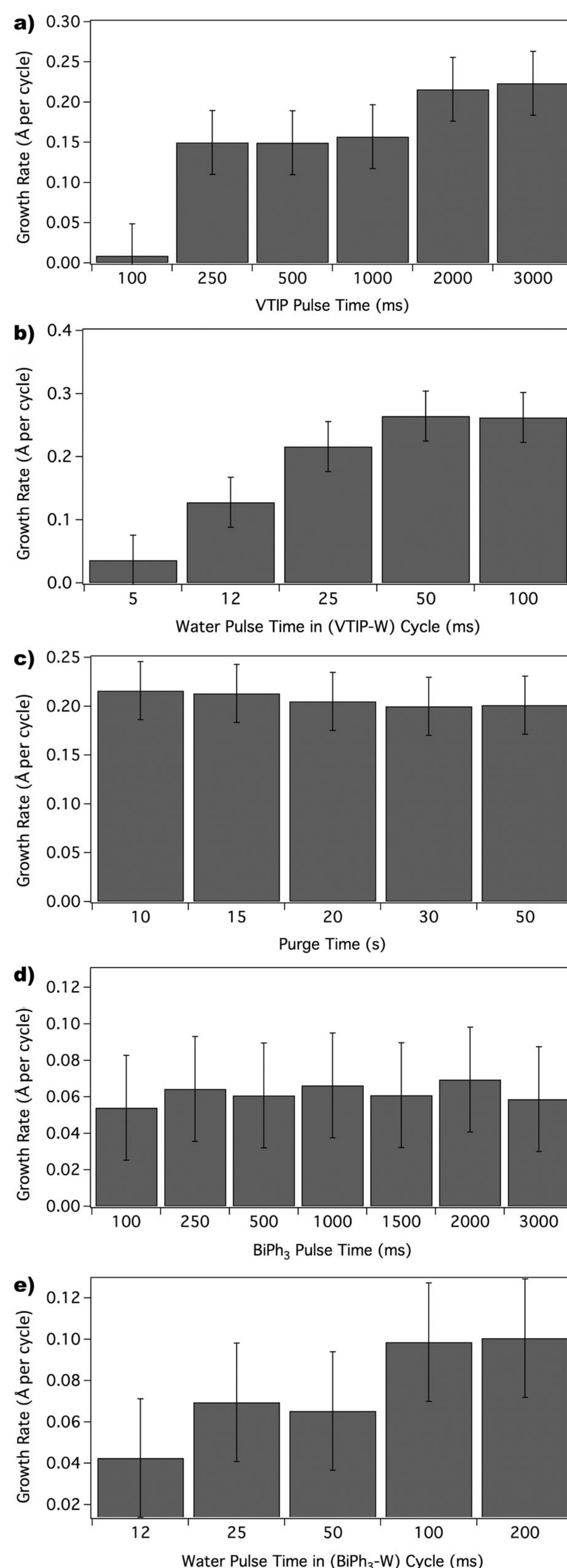

Figure 2. Quartz crystal microbalance (QCM)-measured growth rates from the optimization of ALD parameters. Vanadium oxide growth from the [VTIP–W] cycle as a function of a) VTIP pulse time, b) W pulse time, and c) carrier gas purge time. The parameters for the bismuth cycle were evaluated using the growth rate of [VTIP–W–$BiPh_3$–W] as a proxy since [$BiPh_3$–W] does not result in binary deposition. The bismuth cycle was examined in terms of $BiPh_3$ pulse time (d) and W pulse time (e).

© 2016 Wiley-VCH Verlag GmbH & Co. KGaA, Weinheim

could be reduced to 10 s without significant change in the growth rate per cycle (Figure 2c). As is well known, ALD process conditions vary with reactor design, with the reactor volume, purge rate, and temperature determining the extent of CVD. It was found that VTIP alone resulted in CVD when 1 s exposures were used above 130 °C. The most significant advantage of ALD is its capability to infiltrate porous structures where time is needed for precursor diffusion into and out of the porous films. Thus, subsequent protocol development was limited to a maximum reactor temperature of 130 °C.

Combining multiple ALD processes requires that an overlapping set of conditions be established. The deposition of bismuth vanadates was examined at 130 °C to enable sufficient $BiPh_3$ vapor pressure while staying within the upper limit temperature of 130 °C for ALD growth of V_2O_5. Since the [$BiPh_3$–W] cycle does not result in binary oxide deposition, the pulse parameters were examined using a proxy of the growth rate from the [VTIP–W–$BiPH_3$–W] cycle. A vapor boosting pulse of inert gas was directed into the $BiPH_3$ cylinder just prior to pulsing the precursor into the manifold. The pulse time for $BiPh_3$ was found to not have an effect from 100–3000 ms, indicating that the vapor boosting pulse quickly delivers $BiPh_3$ (Figure 2d). The water pulse length following $BiPH_3$ was found to saturate the growth rate within 25–100 ms (Figure 2e). Again, here using longer than a 25 ms water pulse required extensive purging of 30–60 s to avoid CVD. Thus, 25 ms water pulses allowed the overall ALD process to proceed four times faster. The [VTIP–W–$BiPH_3$–W] cycle was found to result in a reduced deposition rate of 0.07 Å per metal cycle compared to the [VTIP–W] cycle (Figure 1a). The decreased deposition rate in Å per metal cycle is somewhat expected considering the higher density of bismuth vanadates compared to vanadium oxide as bismuth vanadates contain more deposited mass per Å of film thickness. SEM images reveal that the resulting films were relatively smooth and homogeneous in cross-section without apparent pinholes (Figure 1b). Compositional analysis by mass spectrometry identified the deposition of both vanadium and bismuth with a 2.01:1 ratio of V:Bi (Table 1). The significant 33.2 at% Bi in the film was a clear sign of a catalytic effect of a V_2O_5 surface to induce deposition of $BiPh_3$. The metal pulsing ratio was systematically adjusted to tune the composition with [$(VTIP–W)_a$–$(BiPh_3–W)_b$] cycles of variable a:b ratio (Figure 3, Table 1). Increasing the *a*:*b* metal pulsing ratio to 2:1 increased the V:Bi composition ratio to 2.87:1, showing that the second [VTIP–W] cycle deposits efficiently onto the subsequent V_2O_5 surface. However, decreasing the *a*:*b* pulsing ratio to 1:2 resulted in a 1.87:1 composition ratio of V:Bi and slightly increased the bismuth content. This latter result demonstrated, perhaps unsurprisingly, that $BiPh_3$ does not deposit efficiently onto a $BiPh_3$-modified surface. Ozone was examined to improve lysis of the phenyl leaving group. Using ozone, a similar 1:2 pulsing ratio for *a*:*b* resulted in significantly less bismuth content with just 0.04 at% Bi. XRD measurements of as-deposited films from the repeated [VTIP–W–$(BiPH_3–O_3)_2$] cycle exhibited diffraction peaks consistent with crystalline V_2O_5 (Figure S1 in the Supporting Information). Considering that the [VTIP–W–$(BiPh_3–W)_2$] cycle was already shown to deposit bismuth, the substitution of O_3 in the pulse series [VTIP–W–$(BiPh_3–O_3)_2$] apparently led to both the removal of bismuth and the crystallization of V_2O_5. A prior report on V_2O_5 deposition using ozone also noted crystalline films as-deposited at slightly higher temperatures.[58] Different pulse combinations were explored to check for other catalytic combinations of $BiPh_3$ with VTIP. Excluding the oxidant pulse after VTIP with the pulse sequence [VTIP–$BiPh_3$–W] resulted in negligible Bi content of just 1.0 at%, showing that the vanadium isopropoxy surface does not efficiently catalyze deposition from $BiPh_3$. Excluding the oxidant pulse after $BiPh_3$ with the pulse sequence of [VTIP–W–$BiPh_3$] also resulted in very low bismuth content of just 1.1 at%, suggesting that the deposited $BiPh_3$ species is efficiently displaced by subsequent VTIP. These experiments reveal the key combination of [VTIP–W] with [$BiPh_3$–W] for efficient deposition of bismuth vanadates with tunable stoichiometry.

Table 1. Composition of ALD films as-deposited with different pulse sequences.

Pulse sequence	Composition[a] [at%] Bi	V	*X* in BiV_xO_y[b]
[$(VTIP–W)_2$–$BiPh_3$–W]	25.8	74.20	2.87
[VTIP–W–$BiPh_3$–W]	33.2	66.80	2.01 ± 0.08
[VTIP–W–$(BiPh_3–W)_2$]	34.9	65.10	1.87 ± 0.05
[VTIP–W–$(BiPh_3–O_3)_2$]	0.04	99.96	2547
[VTIP–$BiPh_3$–W]	1.0	99.00	100
[VTIP–W–$BiPh_3$]	1.1	98.90	88

[a] On a metals-only basis. [b] Mean ± standard deviation.

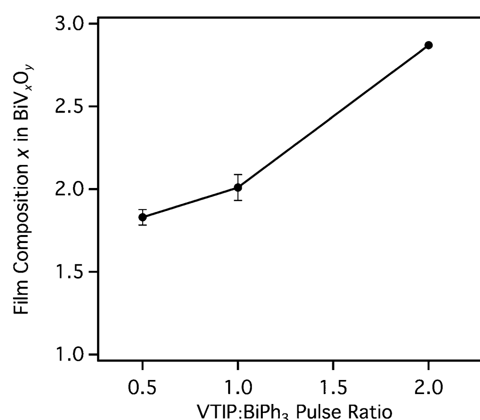

Figure 3. BiV_xO_y composition as measured by mass spectrometry from protocols with different *a*:*b* metal precursor pulsing ratios from repeated cycles of [$(VTIP–W)_a$–$(BiPh_3–W)_b$].

The crystallization of bismuth vanadium oxides was examined after high-temperature calcination treatments. Although the [VTIP–W–$(BiPh_3–W)_2$] cycle produced slightly less V-rich films, the [VTIP–W–$BiPh_3$–W] cycle was used for all subsequent experiments due to its similar composition and significantly faster deposition times. A series of 4000 cycles were used to produce the 55.6 nm thick as-deposited film (Figure 1b). Diffraction measurements on the as-deposited films exhibited a broad amorphous peak (Figure 4a). Some minor loss of vanadium was noted for high temperature treatments (Table 2).

© 2016 Wiley-VCH Verlag GmbH & Co. KGaA, Weinheim

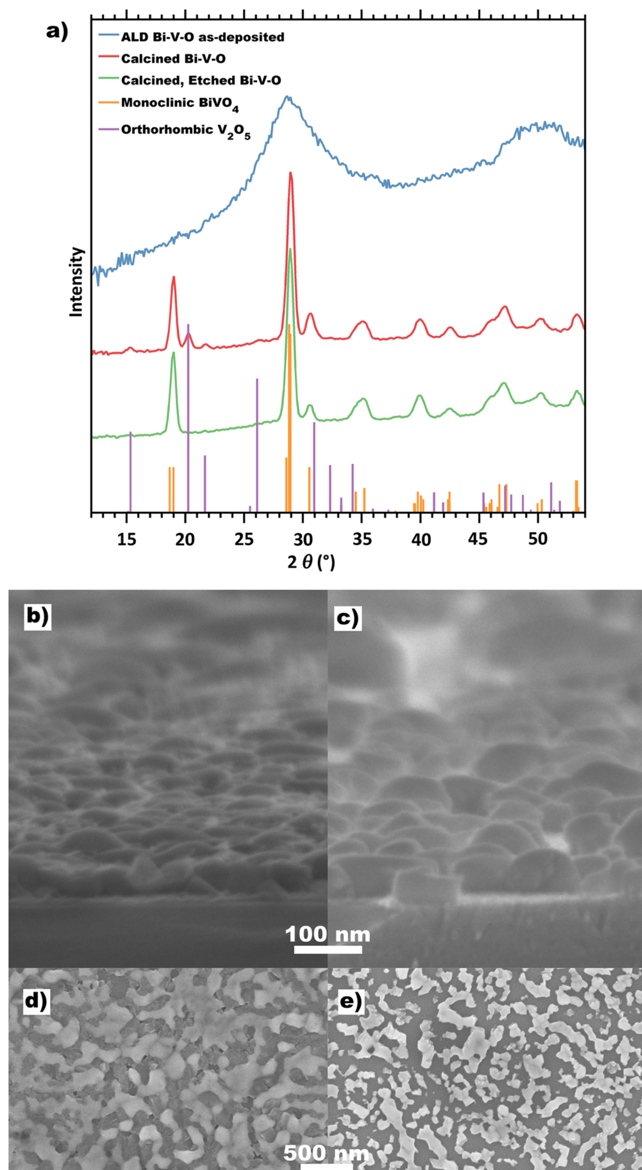

Figure 4. a) X-ray diffraction of Bi–V–O films as-deposited as well as after calcination and subsequent etching (lines are offset vertically for clarity). The allowed peak positions for monoclinic scheelite $BiVO_4$ (PDF#14-0688) and orthorhombic V_2O_5 (PDF# 89-0611) are indicated. SEM imaging confirms that calcination causes spinodal decomposition of the film into $BiVO_4$ and V_2O_5 phases (b,d) and that the subsequent etching leaves behind $BiVO_4$ thin films (c,e).

Table 2. Composition of [VTIP–W–$BiPh_3$–W]$_{4000}$ after subsequent thermal and chemical treatment.

Bi–V–O treatment[a]	Composition[b] [at%] Bi	V	X in BiV_xO_y[c]
calcined	36.6	63.4	1.73±0.17
calcined, etched	51.7	48.3	0.93±0.02

[a] Treatment details can be found in the Experimental Section. [b] On a metals-only basis. [c] Mean±standard deviation.

Considering the vanadium-rich stoichiometry, a vanadium-rich phase from the bismuth–vanadate phase diagram is reasonable to expect. However, the diffraction peaks were well indexed to a mixture of monoclinic scheelite $BiVO_4$ and orthorhombic V_2O_5. The results suggest that vanadium-rich stoichiometries crystallize through spinodal decomposition where the stoichiometric $BiVO_4$ phase forms by phase separation from excess V_2O_5. SEM micrographs of calcined films were consistent with the spinodal decomposition of two phases with additional surface roughness (Figure 4b and d). Please note that the thermal crystallization of conformal amorphous films often results in surface roughness.[8,22,59] Subsequently recorded electrochemical data, vide infra, indicate efficient material performance with good electrical contact to the substrate. BiOI electrochemically deposited by Kim and Choi was calcined using an excess of vanadium salts to produce mixtures of $BiVO_4$ and V_2O_5 where the excess V_2O_5 was subsequently removed by performing a selective base etching.[46] The same etching procedure was applied here to vanadium-rich ALD films after calcination. XRD measurements confirmed the removal of V_2O_5 and identified phase-pure $BiVO_4$ with the scheelite crystal structure and an isotropic distribution of crystallite orientations (Figures 4a and S2). The above conclusions from diffraction data for Bi–V–O films deposited on Si wafers were the same as for films deposited on fluorine-doped tin oxide (FTO), albeit with additional substrate peaks (Figure S3). Mass spectrometry data also confirmed near stoichiometric $BiVO_4$ with a V:Bi stoichiometry of 0.93:1 (Table 2). SEM micrographs of the etched films exhibited an island morphology with voids on the substrate that corresponded to the prior location of phase-separated V_2O_5 (Figure 4c and e). Careful post-processing of bismuth and vanadium-containing ALD films led to the production of phase-pure scheelite $BiVO_4$ with the crystal structure of photoactive scheelite.

The optoelectronic characteristics of bismuth vanadate semiconducting films were examined, both directly after calcination as well as after etching (Figure 5a). As expected for a ~2.4 eV band-gap semiconductor, there was significant absorption occurring for wavelengths less than the band edge of ~520 nm in both films. The as-deposited films were slightly yellow, the calcined films had a pronounced yellow color as is expected for $BiVO_4$, and the etched films were a more transmissive yellow, perhaps due to the loss of some $BiVO_4$ with etching (Figure 5b–d). Minor differences in the optical characteristics were apparent in the band-gap absorption onsets. Tauc analysis assumes a parabolic relationship of energy bands-to-crystal momentum and may be used to measure both direct and indirect band gaps (phonon assisted).[60] A recent study by Cooper et al. conclusively demonstrated that scheelite $BiVO_4$ has an indirect band gap with a direct transition 200 meV above the indirect one.[61] Tauc plots estimated the indirect band gap to be slightly smaller than the expected ~2.4 eV with values of 2.28 and 2.24 eV for the calcined and subsequently etched films, respectively (Figure 5e, Table 3). The direct band gaps were estimated to be ~2.6 eV, similar to previous reports (Figure 5f, Table 3).[61] The fit of each Tauc plot presented was qualitatively similar, although the additional linear region in Figure 5e and the extended absorption beyond 520 nm in Figure 5a suggest the presence of sub-band-gap defect states. Mott–Schottky

© 2016 Wiley-VCH Verlag GmbH & Co. KGaA, Weinheim
These are not the final page numbers!

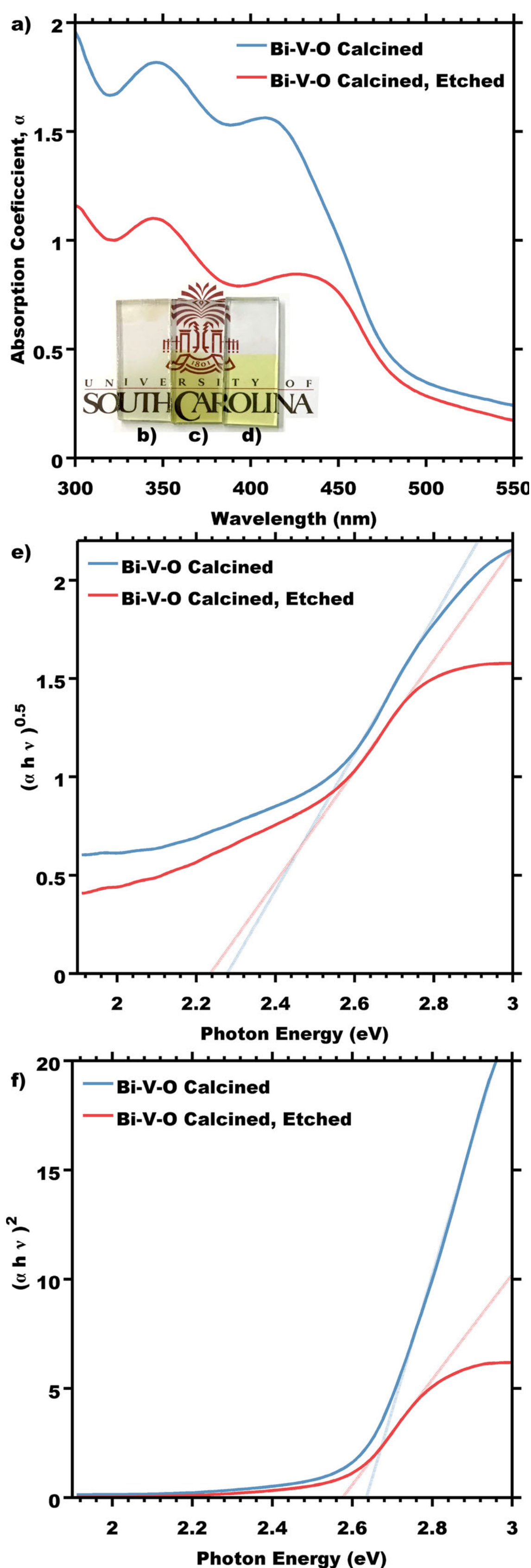

Figure 5. Optoelectronic properties of calcined as well as subsequently etched Bi–V–O films were determined from absorption spectra (a). Inset photos of the Bi–V–O as-deposited (b), calcined (c), and subsequently etched (d) show changes in color and attenuation. Tauc plots for e) indirect and f) direct band gaps were used to estimate the band gaps.

Table 3. Optoelectronic characteristics were extracted from Tauc plots of $[VTIP–W–BiPh_3–W]_{4000}$ films after post treatments.

Sample	Indirect band gap [eV]	Direct band gap [eV]
Bi–V–O calcined	2.28	2.64
Bi–V–O calcined, etched	2.24	2.58

analysis of the films demonstrated the typical ~0 V versus RHE flat band potential with some frequency dependence as was previously observed with doped $BiVO_4$.[52] The etched films consistently had a 16 mV more positive flat-band potential (Figure S4) as well as steeper slopes consistent with a 3:1 reduction in carrier concentration (Table SI). The slight shift in flat-band position and reduced carrier concentration were consistent with reduced doping after etching. Crystalline bismuth vanadate films prepared by ALD were demonstrated to have the expected optoelectronic properties in terms of band-gap and flat-band position.[51,52]

ALD bismuth vanadate films were used for photoelectrochemical water splitting. The films were measured both as-calcined and after a subsequent etching. The photocurrent of any PEC device may be expressed as the product of the light-harvesting efficiency, the charge-separation efficiency, and the charge-injection efficiency.[62] Catalysts were not applied in the present study and thus a hole-scavenging sulfite electrolyte was used to ensure 100% charge injection into the electrolyte. The subsequent photocurrent measurements indicated a potential dependence of the product of the charge separation efficiency with the light-harvesting efficiency.[62] Please note that catalyst modifications have been investigated extensively and are outside the scope of this investigation.[46,49,63,64] Measurements of electrodes in the dark produced negligible current up to 1.4 V versus RHE. Photocurrents of all films exhibited a well-defined onset at 0.35–0.4 V versus RHE with a sloped plateau. The measured photocurrents for as-calcined films were 1.17 ± 0.03 mA cm^{-2} at 1.23 V versus RHE with back-side illumination using a simulated AM 1.5 spectrum (Figure 6). This observed photocurrent of 1.17 mA cm^{-2} is remarkable considering the 55.6 nm thickness of the as-deposited film as compared to <0.35 mA cm^{-2} from <100 nm solid films reported elsewhere.[65–67] The use of many similar efficient layers in host–guest nanocomposites could lead to significant performance gains by improving the overall light-harvesting efficiency. For $BiVO_4$, front-side illumination typically results in much lower photocurrents than back-side illumination owing to low electron conductivity. In contrast, here the front-side and back-side photocurrents were identical within the experimental error (Table 4). This illumination direction independence indicates that the ~50 nm thickness does not measurably impede electron transport capabilities of the resulting $BiVO_4$. Similarly, analysis of differently prepared $BiVO_4$ by van de Krol et al. indicated an electron diffusion length of ~70 nm.[68] After etching, the films all exhibited 17% lower photocurrents on average of 0.97 mA cm^{-2} at 1.23 V versus RHE. Comparison of the absorption profiles before and after etching (Figure 5a) suggests that some $BiVO_4$ may be lost during etching. This minor $BiVO_4$ loss

© 2016 Wiley-VCH Verlag GmbH & Co. KGaA, Weinheim

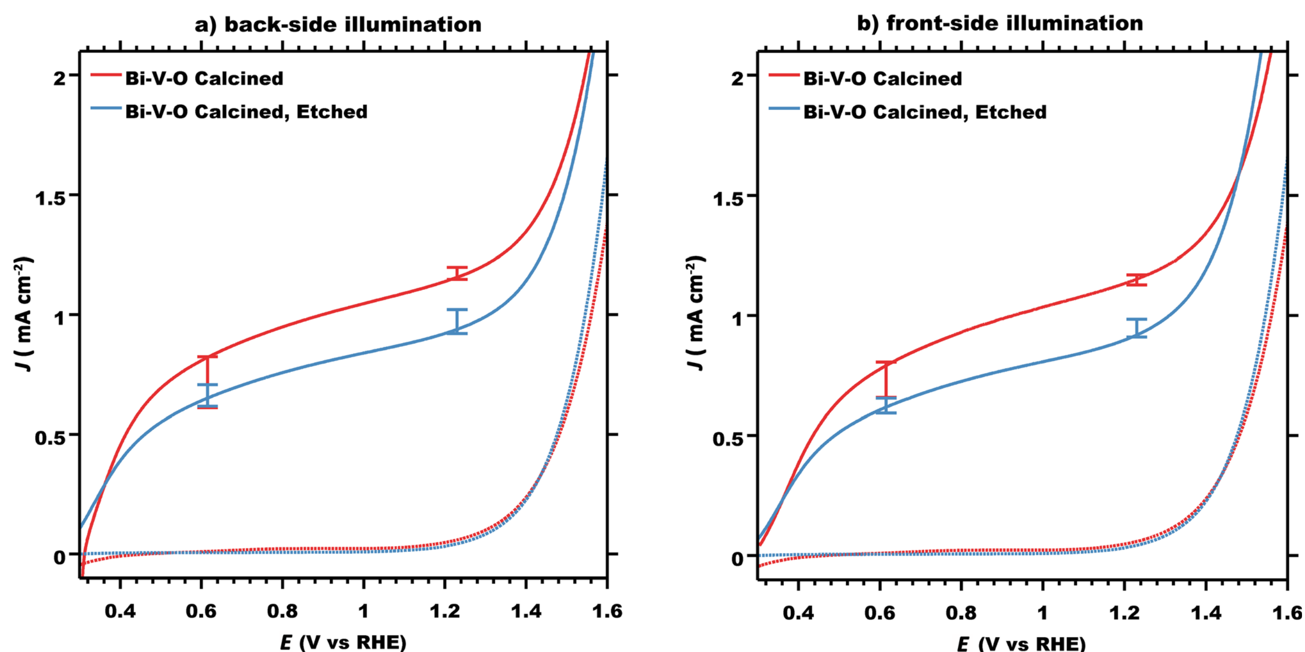

Figure 6. Photoelectrochemical oxidation current vs. potential curves for Bi–V–O films after calcination (red) as well as after subsequent etching (blue). Samples were measured in the dark (dotted lines) and then under simulated AM 1.5 illumination (solid lines). Samples were illuminated through the FTO glass (a) and also through the Bi–V–O film (b). Representative curves are shown with an error bar centered on the average of multiple measurements with the standard deviation indicated. The electrolyte was 0.5 M KH_2PO_4 and 1.0 M Na_2SO_3 at pH 6.8 where the sulfite served as a hole scavenger for films without catalysts.

Table 4. Photoelectrochemical performance of bismuth vanadate films $[VTIP\text{-}W\text{-}BiPh_3\text{-}W]_{4,000}$ subjected to different treatments.

Sample	Front-side illumination $J^{[a]}$ [mA cm^{-2}]@0.615 V	$J^{[a]}$ [mA cm^{-2}]@1.23 V	Back-side illumination $J^{[a]}$ [mA cm^{-2}]@0.615 V	$J^{[a]}$ [mA cm^{-2}]@1.23 V
Bi–V–O calcined	0.73 ± 0.07	1.15 ± 0.02	0.70 ± 0.11	1.17 ± 0.03
Bi–V–O calcined, etched	0.62 ± 0.03	0.95 ± 0.04	0.66 ± 0.04	0.97 ± 0.05

[a] Mean ± standard deviation reported for 4 devices measured in pH 6.8 electrolyte with sulfite hole-scavenger under simulated AM 1.5 illumination; potentials are vs. RHE.

is reasonable to expect as spinodal decomposition randomly places some V_2O_5 between $BiVO_4$ and the FTO contact. Integration of the absorption profiles with the AM 1.5 spectrum yielded theoretical photocurrent limits of 4.28 and 3.38 mA cm^{-2} for the calcined and etched films, respectively. These theoretical photocurrents correspond to 56.7% and 44.8% light-harvesting efficiency for the calcined and etched films, respectively, based upon the 7.55 mA cm^{-2} limit for $BiVO_4$ absorbing all of the AM 1.5 spectrum up to the 2.4 eV band gap. Taking into account the different light-harvesting efficiencies, the measured photocurrents indicate that both film preparation conditions have a charge separation efficiency of ~28% that is comparable to similar undoped, solid $BiVO_4$ films.[45] Thus, the difference in performance was attributed to differences in light-harvesting efficiency. Unlike thick films that are limited by charge diffusion, such thin films often have lower charge separation efficiencies due to the dominance of interfacial effects and trapping states.[69] ALD has previously been used to modify the FTO–absorber interface[21] and provides an ideal method to mitigate this challenge in future studies. It is reasonable to expect that the rare $BiVO_4$ clusters with only V_2O_5 contacts could contribute to the photocurrent by passing electrons via the slightly lower V_2O_5 conduction band.[70,71] V_2O_5 is reported to have a band gap ranging from 2.3–2.8 eV, which could also account for some of the light-harvesting losses upon etching. The stability of bismuth vanadate films was examined in detail elsewhere.[45,72–74] The ALD bismuth vanadate films reported here were found to slowly decrease in performance with ~20% photocurrent reduction for both conditions after 2 h of continuous operation under simulated AM 1.5 illumination at a potential of 1.23 V versus RHE (Figure S5). For both conditions, ALD bismuth vanadate films produced significant photocurrents. Further optimization of the defect structures and internal quantum efficiencies will enable advances to the state-of-the-art for water splitting using bismuth vanadate with host–guest nanostructures.

Conclusions

The deposition of $BiVO_4$ guests on arbitrary host materials is crucial for the advancement of solar water splitting using thin-absorbers within host–guest architectures. Uniformity is impor-

© 2016 Wiley-VCH Verlag GmbH & Co. KGaA, Weinheim

tant for future fundamental studies of material performance. Likewise, the capability to deposit $BiVO_4$ by atomic layer deposition (ALD) also enables the examination of diverse host materials without imposing a requirement of sufficient conductivity for electrodeposition, for example. The atomic layer deposition of bismuth vanadates are reported from $BiPh_3$, vanadium(V) oxytriisopropoxide (VTIP), and water. The films had tunable stoichiometry and were crystallized to form the photoactive scheelite structure of $BiVO_4$. The resulting films were shown to be highly photoactive under AM 1.5 illumination with average photocurrents of $1.17\ mA\,cm^{-2}$ at 1.23 V versus reversible hydrogen electrode. The high water-splitting photocurrent for a single thin-film layer of $BiVO_4$ lays the ground work for elaboration of efficient multi-layer devices with host–guest architectures.

Experimental Section

Materials. Triphenyl bismuth ($BiPh_3$, 99%) and vanadium(V) tri-isopropoxy oxide, (VTIP, 98+%) were used as received from STREM. Deionized (DI) water was prepared using a Siemens Labostar model. Isopropanol (70% lab grade, BDH), KH_2PO_4 (Reagent Grade, Fisher), Na_2SO_3 (ACS Grade, Macron), KOH (ACS Grade, Fisher), and H_3BO_3 (ACS Grade, Fisher) were used as-received. TEC-15 fluorine-doped tin oxide coated glass (FTO) was purchased from Hartford Glass. The FTO substrates were cleaned extensively before use with isopropanol and DI water before sonication in soapy water (Decon Contrex, 2 wt%), followed by additional rinses with water and isopropanol, followed by sonication in isopropanol. The cleaned FTO substrates were then calcined using a Barnstead Thermolyne muffle furnace at 450°C for 1 h just prior to use. Polished n-doped silicon wafers with (100) orientation were purchased from University Wafers, USA. High-temperature grade Kapton tape was purchased from McMaster-CARR, USA. Ultra-high purity nitrogen (99.999%) and oxygen (99.5%) were used as received from Praxair.
Atomic layer deposition. Samples were masked using Kapton tape to define the deposition region. Samples for composition analysis were masked on the bottom to avoid diffusion gradients along the back of the films. Samples on FTO were masked on the back as well as partially on the front to provide clean electrical contacts for PEC measurements. The $BiPh_3$ and VTIP were each loaded into separate stainless steel cylinders in an argon glovebox. Water was loaded into a stainless steel cylinder under normal atmosphere. The cylinders were sealed and then connected to an Arradiance Gemstar-8 reactor. Nitrogen was used as the carrier gas as well as the purging gas. Precursor dosing was controlled using Swagelok ALD valves. The $BiPh_3$ and VTIP cylinders were heated to 130 and 45°C, respectively. Unless otherwise noted, the reactor was set to 130°C, both metal precursors had a pulse time of 2 s, and water had a pulse time of 25 ms. Ozone was used for a few experiments with an oxygen flow rate of $0.5\ L\,min^{-1}$ through a Nano ozone generator (Ozone Solutions, USA), producing a continuous stream of 12% O_3. A vapor-boosting 20 ms pulse of nitrogen was added to the $BiPh_3$ cylinder just prior to each pulse. The reactor chamber was isolated before each pulse to contain the precursors for 1 s after exposure ("exposure mode"). Unless noted otherwise, the excess precursors were purged after each exposure using 200 sccm nitrogen for 10 s. The deposition protocols were organized into a V_2O_5 loop and a Bi_2O_3 loop for an overall cycle of $[(VTIP–W)_a–(BiPh_3–W)_b]_c$ where the *a*/*b* ratio was used to control composition and *c* controlled the total thickness deposited. A comprehensive ALD protocol is provided in the Supporting Information.
In situ deposition monitoring. An array of quartz crystal microbalances (QCMs) were used to monitor ALD depositions in situ across the reaction chamber. Please note that while data were recorded in real time, the pulsing of precursors, varying flow rates, and proportional-integral-derivative (PID) controller cycles caused thermal transients that obfuscated the very small signals for mass change during individual pulses. Thus, average deposition rates were determined using a least squares fit optimization for the linear deposition rate. A total of 500–8000 ALD cycles were performed for each experiment to provide accurate measurements of growth per cycle. The standard deviation for growth rates was estimated using repeated measurements. A standard deviation of 0.039 Å per cycle was determined for V_2O_5 and 0.028 Å per cycle for BiV_xO_y. The QCM crystals were installed in a low-profile plate inside the deposition chamber with electrical connections fed through an auxiliary port. The custom-designed QCM array (Colnatec) utilized a special sealing interface to eliminate the need for inert gas purging on the backside of the crystals. Such purging-based designs were shown to work well.[75,76] Radiation-compensated (RC) cut quartz crystals were used with aluminum contacts (Colnatec). The native oxide on the aluminum top-contact of the QCM crystals led to the facile establishment of linear QCM responses. In contrast, gold-coated QCM crystals showed initially nucleation-limited deposition. QCM deposition data were calibrated per SEM observations of film thickness.
Composition analysis. Samples were digested in 5 mL of 4 M nitric acid (Fisher, Optima grade) in Teflon vessels at 180°C for 5 h. The resulting solution was diluted to 50 mL using deionized water. A Finnigan ELEMENT XR double-focusing magnetic sector field–inductively coupled plasma–mass spectrometer (SF–ICP–MS) was used for the analysis of V (51, LR), Bi (209, LR), and internal standard Rh (103 LR). A Micromist U-series nebulizer (GE, Australia) was operated at $0.2\ mL\,min^{-1}$ with a quartz torch and an injector (Thermo Fisher Scientific, USA) for sample introduction. The gas flow was set to $1.08\ mL\,min^{-1}$. The forwarding power was 1250 W. Composition analysis was based on a five-point calibration curve for both V and Bi. The calibration range was from 10 to 600 ppb. The R^2 values for the initial calibration curves were greater than 0.999.
Film treatments. The ALD films were heated to induce crystallization. Samples were heated at $5\,°C\,min^{-1}$ to 200°C, followed by $2\,°C\,min^{-1}$ to 450°C, held constant at 450°C for 10 h, and then finally were allowed to cool in the furnace. Some films were subsequently etched for 20 min in 1 M NaOH to remove V_2O_5.
Diffraction. X-ray diffraction experiments were conducted using a SAXSLab Ganesha at the South Carolina SAXS Collaborative. A Xenocs GeniX3D microfocus source was used with a Cu target to generate a monochromatic beam with a 0.154 nm wavelength. The instrument was calibrated using silicon powder (NIST 640e). Scattering data were processed from the scattering vector $q = 4\pi\lambda^{-1}\sin\theta$ where λ is the X-ray wavelength and 2θ is the total scattering angle. A Pilatus 300 K detector (Dectris) was used to collect the two-dimensional (2D) scattering patterns. Samples were measured at an incident angle of 8° relative to the film plane. SAXS GUI software was used to radially integrate the 2D patterns to reduced 1D profiles. The conversion of the resulting intensity versus *q* data was converted to 2θ using the above formula.
Photoelectrochemical and electrochemical measurements. Linear sweep voltammograms were measured using a three-electrode potentiostat (Biologic SP-150) with a Ag/AgCl/KCL 4.0 M reference electrode (Pine Instruments) and a platinum wire counter electrode (Pine Instruments). Samples on FTO substrates were clamped with

© 2016 Wiley-VCH Verlag GmbH & Co. KGaA, Weinheim

a titanium sheet to provide an ohmic contact. The electrodes were placed into a cell made of polyether ether ketone (PEEK) with a fused-silica window. Simulated sunlight was generated using a 75 W xenon lamp (OBB, Horiba) that passed through a water infrared filter (OBB, Horiba), a KG-3 filter (315–710 nm pass, Edmund Optics), and finally a BG-40 filter with an antireflective coating (335–610 nm pass, Thor Labs). This combination of filters removed much of the UV light where a Xe lamp has the most spectral mismatch from the AM 1.5 spectrum. The transmitted light was collimated using a fused-silica lens (Thor Labs) and then passed through an engineered diffuser with a top-hot profile to provide a homogeneous intensity profile with a slight 10° divergence. The transmitted light was corrected for brightness in the 335–610 nm spectral range to generate a photocurrent identical to AM 1.5 sunlight. The illumination intensity was measured using a calibrated UV-enhance Silicon photodiode (Thorlabs) equipped with a neutral reflective filter (optical density 1.0, Thorlabs) to maintain a linear and calibrated photodiode response. This calibration practice provides accurate solar simulation in terms of both spectral distribution and brightness with a minimal correction factor.[77]

Linear sweep voltammograms were measured in an electrolyte containing 0.5 м KH_2PO_4 and 1.0 м Na_2SO_3 at pH 6.8 as confirmed by a calibrated Thermoscientific Orionstar A211 pH meter. The sulfite acted as a hole scavenger to provide quantitative charge injection from the semiconductor to the electrolyte for the measurement of film performance without catalysts. The samples were scanned from −0.400 to 1.0 V (vs. Ag/AgCl reference electrode) at 10 mV s^{-1}. Multiple scans were completed at each condition to confirm reproducibility and the second scan results were reported. Chronoamperometry measurements were made using an electrolyte containing 0.5 м H_3BO_3 and 0.2 м Na_2SO_3 adjusted to pH 9.26 with KOH.[74] Staircase potentio-electrochemical impedance spectroscopy (EIS) was performed in the dark using an electrolyte containing 0.5 м H_3BO_3 that was adjusted to pH 9.4 with KOH and then sparged with nitrogen continuously during measurements. A perturbation of 10 mV was used for EIS over a range of frequencies. The recorded reactance was directly used to calculate the approximate capacitance as a function of voltage. All electrochemical potentials E were reported versus the reversible hydrogen electrode (RHE) using the formula E(vs. RHE) = E(vs. Ag/AgCl) + E_{ref}(Ag/AgCl) + 0.059 V*pH where E_{ref} = 0.201 V in this case.

Optoelectronic properties. The optical response of thin films was measured using a Shimadzu UV-2450. A sandwich configuration of FTO–water–fused quartz was used to minimize light-scattering differences between the blank measurement of bare FTO and samples coated onto FTO. The illumination direction was through the glass of the FTO. Identical measurements on bare FTO were used to establish the baseline for the measurement of the optical properties of the deposited films alone.

Morphology. A Zeiss Ultra Plus scanning electron microscope (SEM) was operated at 5 kV using an in-lens secondary electron detector to observe the film surface and cross-sectional morphologies. Fresh edges were fractured for each cross-sectional acquisition. ALD growth rates were calculated based upon cross-sectional SEM imaging of films in the 50–100 nm thickness range.

Acknowledgements

M.S. acknowledges the University of South Carolina for startup funds. This work made use of the South Carolina SAXS Collaborative, supported by the NSF Major Research Instrumentation program (award #DMR-1428620). I thank Arradiance for their dedicated ALD support and Colnatec for the design of a custom low-profile QCM array. I thank Lijian He and the Mass Spectrometry Center at USC for assistance with composition analysis.

Keywords: atomic layer deposition · bismuth · energy conversion · vanadates · water splitting

[1] T. Suntola, *Thin Solid Films* **1992**, *216*, 84.
[2] S. M. George, A. W. Ott, J. W. Klaus, *J. Phys. Chem.* **1996**, *100*, 13121.
[3] M. Ritala, M. Leskela, J.-P. Dekker, C. Mutsaers, P. J. Soininen, J. Skarp, *Chem. Vap. Deposition* **1999**, *5*, 7.
[4] C. Detavernier, J. Dendooven, S. P. Sree, K. F. Ludwig, J. A. Martens, *Chem. Soc. Rev.* **2011**, *40*, 5242.
[5] A. F. Palmstrom, P. K. Santra, S. F. Bent, *Nanoscale* **2015**, *7*, 12266.
[6] T. Wang, Z. Luo, C. Li, J. Gong, *Chem. Soc. Rev.* **2014**, *43*, 7469.
[7] Y. Lin, G. Yuan, S. Sheehan, S. Zhou, D. Wang, *Energy Environ. Sci.* **2011**, *4*, 4862.
[8] Y. Lin, S. Zhou, S. W. Sheehan, D. Wang, *J. Am. Chem. Soc.* **2011**, *133*, 2398.
[9] Y. Lin, Y. Xu, M. T. Mayer, Z. I. Simpson, G. McMahon, S. Zhou, D. Wang, *J. Am. Chem. Soc.* **2012**, *134*, 5508.
[10] M. T. Mayer, C. Du, D. Wang, *J. Am. Chem. Soc.* **2012**, *134*, 12406.
[11] T. Hamann, *Dalton Trans.* **2012**, *41*, 7830.
[12] B. Klahr, S. Gimenez, F. Fabregat-Santiago, J. Bisquert, T. W. Hamann, *Energy Environ. Sci.* **2012**, *5*, 7626.
[13] O. Zandi, B. M. Klahr, T. W. Hamann, *Energy Environ. Sci.* **2013**, *6*, 634.
[14] K. M. Young, T. W. Hamann, *Chem. Commun.* **2014**, *50*, 8727.
[15] O. Zandi, J. A. Beardslee, T. Hamann, *J. Phys. Chem. C* **2014**, *118*, 16494.
[16] O. Zandi, T. W. Hamann, *J. Phys. Chem. Lett.* **2014**, *5*, 1522.
[17] F. Le Formal, N. Tétreault, M. Cornuz, T. Moehl, M. Grätzel, K. Sivula, *Chem. Sci.* **2011**, *2*, 737.
[18] T. Hisatomi, F. Le Formal, M. Cornuz, J. Brillet, N. Tétreault, K. Sivula, M. Grätzel, *Energy Environ. Sci.* **2011**, *4*, 2512.
[19] L. Steier, I. Herraiz-Cardona, S. Gimenez, F. Fabregat-Santiago, J. Bisquert, S. D. Tilley, M. Grätzel, *Adv. Funct. Mater.* **2014**, *24*, 7681.
[20] L. Steier, J. Luo, M. Schreier, M. T. Mayer, T. Sajavaara, M. Grätzel, *ACS Nano* **2015**, *9*, 11775.
[21] T. Hisatomi, H. Dotan, M. Stefik, K. Sivula, A. Rothschild, M. Grätzel, N. Mathews, *Adv. Mater.* **2012**, *24*, 2699.
[22] M. Stefik, M. Cornuz, N. Mathews, T. Hisatomi, S. Mhaisalkar, M. Grätzel, *Nano Lett.* **2012**, *12*, 5431.
[23] S. C. Riha, M. J. Vermeer, M. J. Pellin, J. T. Hupp, A. B. Martinson, *ACS Appl. Mater. Interfaces* **2013**, *5*, 360.
[24] J. A. Klug, N. G. Becker, S. C. Riha, A. B. F. Martinson, J. W. Elam, M. J. Pellin, T. Proslier, *J. Mater. Chem. A* **2013**, *1*, 11607.
[25] S. C. Riha, J. M. Racowski, M. P. Lanci, J. A. Klug, A. S. Hock, A. B. Martinson, *Langmuir* **2013**, *29*, 3439.
[26] Y. Qiu, S. F. Leung, Q. Zhang, B. Hua, Q. Lin, Z. Wei, K. H. Tsui, Y. Zhang, S. Yang, Z. Fan, *Nano Lett.* **2014**, *14*, 2123.
[27] A. Paracchino, V. Laporte, K. Sivula, M. Grätzel, E. Thimsen, *Nat. Mater.* **2011**, *10*, 456.
[28] A. Paracchino, N. Mathews, T. Hisatomi, M. Stefik, S. D. Tilley, M. Grätzel, *Energy Environ. Sci.* **2012**, *5*, 8673.
[29] S. D. Tilley, M. Schreier, J. Azevedo, M. Stefik, M. Grätzel, *Adv. Funct. Mater.* **2014**, *24*, 303.
[30] J. Azevedo, L. Steier, P. Dias, M. Stefik, C. T. Sousa, J. P. Araújo, A. Mendes, M. Grätzel, S. D. Tilley, *Energy Environ. Sci.* **2014**, *7*, 4044.
[31] S. Hu, M. R. Shaner, J. A. Beardslee, M. Lichterman, B. S. Brunschwig, N. S. Lewis, *Science* **2014**, *344*, 1005.
[32] Z. F. Huang, J. Song, L. Pan, X. Zhang, L. Wang, J. J. Zou, *Adv. Mater.* **2015**, *27*, 5309.
[33] B. M. Kayes, H. A. Atwater, N. S. Lewis, *J. Appl. Phys.* **2005**, *97*, 114302.
[34] J. R. Maiolo, B. M. Kayes, M. A. Filler, M. C. Putnam, M. D. Kelzenberg, H. A. Atwater, N. S. Lewis, *J. Am. Chem. Soc.* **2007**, *129*, 12346.
[35] S. W. Boettcher, J. M. Spurgeon, M. C. Putnam, E. L. Warren, D. B. Turner-Evans, M. D. Kelzenberg, J. R. Maiolo, H. A. Atwater, N. S. Lewis, *Science* **2010**, *327*, 185.

© 2016 Wiley-VCH Verlag GmbH & Co. KGaA, Weinheim

[36] I. Kondofersky, H. K. Dunn, A. Müller, B. Mandlmeier, J. M. Feckl, D. Fattakhova-Rohlfing, C. Scheu, L. M. Peter, T. Bein, *ACS Appl. Mater. Interfaces* **2015**, *7*, 4623.
[37] K. Sivula, F. L. Formal, M. Grätzel, *Chem. Mater.* **2009**, *21*, 2862.
[38] Y. Pihosh, I. Turkevych, K. Mawatari, T. Asai, T. Hisatomi, J. Uemura, M. Tosa, K. Shimamura, J. Kubota, K. Domen, T. Kitamori, *Small* **2014**, *10*, 3692.
[39] L. Zhang, E. Reisner, J. J. Baumberg, *Energy Environ. Sci.* **2014**, *7*, 1402.
[40] J. Su, L. Guo, N. Bao, C. A. Grimes, *Nano Lett.* **2011**, *11*, 1928.
[41] F. D. Hardcastle, I. E. Wachs, H. Eckert, D. A. Jefferson, *J. Solid-State Chem.* **1991**, *90*, 194.
[42] K. V. R. Prasad, K. B. R. Varma, *J. Phys. D* **1991**, *24*, 1858.
[43] K. V. R. Prasad, K. B. R. Varma, A. R. Raju, K. M. Satyalakshmi, R. M. Mallya, M. S. Hegde, *Appl. Phys. Lett.* **1993**, *63*, 1898.
[44] K. V. R. Prasad, A. R. Raju, K. B. R. Varma, *J. Mater. Sci.* **1994**, *29*, 2691.
[45] F. F. Abdi, L. Han, A. H. Smets, M. Zeman, B. Dam, R. van de Krol, *Nat. Commun.* **2013**, *4*, 2195.
[46] T. W. Kim, K. S. Choi, *Science* **2014**, *343*, 990.
[47] Z. F. Huang, L. Pan, J. J. Zou, X. Zhang, L. Wang, *Nanoscale* **2014**, *6*, 14044.
[48] X. Shi, I. Y. Choi, K. Zhang, J. Kwon, D. Y. Kim, J. K. Lee, S. H. Oh, J. K. Kim, J. H. Park, *Nat. Commun.* **2014**, *5*, 4775.
[49] Y. Pihosh, I. Turkevych, K. Mawatari, J. Uemura, Y. Kazoe, S. Kosar, K. Makita, T. Sugaya, T. Matsui, D. Fujita, M. Tosa, M. Kondo, T. Kitamori, *Sci. Rep.* **2015**, *5*, 11141.
[50] A. Kudo, K. Ueda, H. Kato, I. Mikami, *Catal. Lett.* **1998**, *53*, 229.
[51] S. Tokunaga, H. Kato, A. Kudo, *Chem. Mater.* **2001**, *13*, 4624.
[52] Y. Park, D. Kang, K.-S. Choi, *Phys. Chem. Chem. Phys.* **2014**, *16*, 1238.
[53] R. Saito, Y. Miseki, K. Sayama, *Chem. Commun.* **2012**, *48*, 3833.
[54] T. Hatanpää, M. Vehkamaki, M. Ritala, M. Leskela, *Dalton Trans.* **2010**, *39*, 3219.
[55] M. Vehkamäki, T. Hatanpaa, M. Ritala, M. Leskela, *J. Mater. Chem.* **2004**, *14*, 3191.
[56] M. Schuisky, K. Kukli, M. Ritala, A. Harsta, M. Leskela, *Chem. Vap. Deposition* **2000**, *6*, 139.
[57] J. C. Badot, *Electrochem. Solid-State Lett.* **1999**, *3*, 485.
[58] X. Chen, E. Pomerantseva, P. Banerjee, K. Gregorczyk, R. Ghodssi, G. Rubloff, *Chem. Mater.* **2012**, *24*, 1255.
[59] V. Miikkulainen, M. Leskela, M. Ritala, R. L. Puurunen, *J. Appl. Phys.* **2013**, *113*, 021301.
[60] J. Tauc, R. Grigorovici, A. Vancu, *phys. stat. sol. b* **1966**, *15*, 627.
[61] J. K. Cooper, S. Gul, F. M. Toma, L. Chen, Y.-S. Liu, J. Guo, J. W. Ager, J. Yano, I. D. Sharp, *J. Phys. Chem. C* **2015**, *119*, 2969.
[62] H. Dotan, K. Sivula, M. Grätzel, A. Rothschild, S. C. Warren, *Energy Environ. Sci.* **2011**, *4*, 958.
[63] S. K. Pilli, T. E. Furtak, L. D. Brown, T. G. Deutsch, J. A. Turner, A. M. Herring, *Energy Environ. Sci.* **2011**, *4*, 5028.
[64] F. F. Abdi, N. Firet, R. van de Krol, *ChemCatChem* **2013**, *5*, 490.
[65] E. Alarcón-Lladó, L. Chen, M. Hettick, N. Mashouf, Y. Lin, A. Javey, J. W. Ager, *Phys. Chem. Chem. Phys.* **2014**, *16*, 1651.
[66] M. Li, L. Zhao, L. Guo, *Int. J. Hydrogen Energy* **2010**, *35*, 7127.
[67] S. Hernández, S. M. Thalluri, A. Sacco, S. Bensaid, G. Saracco, N. Russo, *Appl. Catal. A* **2015**, *504*, 266.
[68] F. F. Abdi, T. J. Savenije, M. M. May, B. Dam, R. van de Krol, *J. Phys. Chem. Lett.* **2013**, *4*, 2752.
[69] F. Le Formal, M. Grätzel, K. Sivula, *Adv. Funct. Mater.* **2010**, *20*, 1099.
[70] Y. Xu, M. A. A. Schoonen, *Am. Mineral.* **2000**, *85*, 543.
[71] H. Jiang, M. Nagai, K. Kobayashi, *J. Alloys Compd.* **2009**, *479*, 821.
[72] K. J. McDonald, K.-S. Choi, *Energy Environ. Sci.* **2012**, *5*, 8553.
[73] M. T. McDowell, M. F. Lichterman, J. M. Spurgeon, S. Hu, I. D. Sharp, B. S. Brunschwig, N. S. Lewis, *J. Phys. Chem. C* **2014**, *118*, 19618.
[74] Y. Kuang, Q. Jia, H. Nishiyama, T. Yamada, A. Kudo, K. Domen, *Adv. Energy Mater.* **2016**, *6*, 1501645.
[75] J. W. Elam, M. D. Groner, S. M. George, *Rev. Sci. Instrum.* **2002**, *73*, 2981.
[76] S. C. Riha, J. A. Libera, J. W. Elam, A. B. Martinson, *Rev. Sci. Instrum.* **2012**, *83*, 094101.
[77] C. H. Seaman, *Solar Energy* **1982**, *29*, 291.

Received: April 7, 2016
Published online on ■■ ■■, 0000

 © 2016 Wiley-VCH Verlag GmbH & Co. KGaA, Weinheim

M. Stefik*

■■–■■

Atomic Layer Deposition of Bismuth Vanadates for Solar Energy Materials

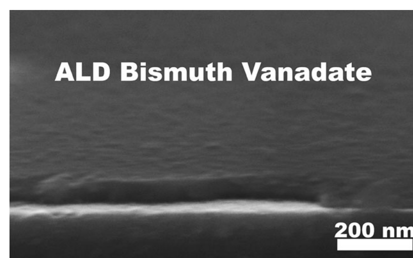

Solar Energy Materials: Bismuth vanadates of tunable composition are fabricated using atomic layer deposition (ALD). ALD allows the first production of bismuth vanadates deposited in a conformal fashion onto arbitrary substrates. The films are calcined to yield the photoactive scheelite phase and are capable of efficient solar-assisted water splitting with thin-film photocurrents greater than 1 mA cm^{-2} under simulated AM 1.5 illumination.

© 2016 Wiley-VCH Verlag GmbH & Co. KGaA, Weinheim
These are not the final page numbers!